

ARTICLE OPEN

Transport anomalies in the layered compound BaPt₄Se₆

Sheng Li¹, Yichen Zhang², Hanlin Wu¹, Huifei Zhai¹, Wenhao Liu¹, Daniel Peirano Petit¹, Ji Seop Oh^{2,3}, Jonathan Denlinger⁴, Gregory T. McCandless⁵, Julia Y. Chan⁶, Robert J. Birgeneau^{3,6}, Gang Li⁷, Ming Yi^{2✉} and Bing Lv^{1✉}

We report a layered ternary selenide BaPt₄Se₆ featuring sesqui-selenide Pt₂Se₃ layers sandwiched by Ba atoms. The Pt₂Se₃ layers in this compound can be derived from the Dirac-semimetal PtSe₂ phase with Se vacancies that form a honeycomb structure. This structure results in a Pt (VI) and Pt (II) mixed-valence compound with both PtSe₆ octahedra and PtSe₄ square net coordination configurations. Temperature-dependent electrical transport measurements suggest two distinct anomalies: a resistivity crossover, mimic to the metal-insulator (M-I) transition at ~150 K, and a resistivity plateau at temperatures below 10 K. The resistivity crossover is not associated with any structural, magnetic, or charge order modulated phase transitions. Magnetoresistivity, Hall, and heat capacity measurements concurrently suggest an existing hidden state below 5 K in this system. Angle-resolved photoemission spectroscopy measurements reveal a metallic state and no dramatic reconstruction of the electronic structure up to 200 K.

npj Quantum Materials (2021)6:80; <https://doi.org/10.1038/s41535-021-00382-x>

INTRODUCTION

Two-dimensional (2D) transition metal dichalcogenides (TMDs), with various polytype structures such as 1T, 1T', 2H, and 3R phases, have provided a fertile ground for fundamental quantum materials research and emergent potential applications in the past decade due to the fascinating physical properties discovered in these materials^{1–17}. In most cases, structural defects such as vacancies and grain boundaries disrupt the translational symmetry of these pristine lattices and significantly impact their physical and chemical properties. Typically, these defects are detrimental to the carrier mobility and associated charge transport performance^{18–20}. However, defect engineering through carefully controlled atomic defects has recently emerged as a versatile and effective tool that can significantly improve the physical properties, tune the electronic structures, and tailor their device performances for 2D materials. It has been demonstrated that different types of controlled defect structures have led to the enhancement of electrical transport, optical, and chemical properties, for various TMD materials^{21–23}. If such defects are well-ordered, a new type of structure or even unprecedented physical properties could also be developed^{24,25}. For example, Mo₆Te₆ nanowire forms at the boundaries of 2H-MoTe₂ through thermal annealing under vacuum²⁶; novel Mo₂S₃ is fabricated through a periodic assembly of chalcogen vacancy lines in the corresponding MoS₂ monolayers²⁷. Point defects and line defects of chalcogen atoms induce magnetism in PtSe₂ and ReS₂ where magnetism does not exist in the pristine materials^{28,29}. Besides defect engineering, chemical intercalation that introduces guest species into the van der Waals gaps can also effectively change the band filling and the chemical potential of TMD materials and lead to drastic changes in their electronic, transport, and optical properties^{30–32}. These intercalates can range from cations, anions, neutral atoms, and even organic molecules, and could also introduce charge orders^{33,34}, superconductivity^{35,36}, or magnetic orders^{37,38} into the host TMD materials.

Among the known TMDs, PtSe₂ has been well-known for its high performance in photocatalysis, electrocatalysis, and high mobility in field-effect transistors^{39–45}. With dimension reduction of PtSe₂, the physical properties will change from that of a bulk Dirac-semimetal to a monolayer semiconductor with an indirect bandgap of 1.2 eV⁴⁶. Different types of defects have been found in the bulk and thin films of PtSe₂, and they have experimentally and theoretically impacted the related properties^{28,47}. Thickness-independent semiconducting-to-metallic conversion, in contrast to semiconducting-to-metal transition with reduced thickness, has been observed through plasma-driven atomic defect engineering in PtSe₂ films⁴⁸. Theoretical calculations suggested that large spin-orbit splitting can be induced by introducing point defects in the PtSe₂⁴⁹, and the Se vacancy line defects in monolayer PtSe₂ could cause a sizable spin splitting in the defect states⁵⁰. This large spin-orbital splitting gives rise to persistent spin textures, which protect the spin from decoherence and induce an extraordinarily long spin lifetime for designing spintronic devices.

As a part of chemical doping studies with controlled defects synthesis for bulk PtSe₂ materials⁵¹, we report herein a ternary compound of BaPt₄Se₆ of layered structure featured with sesqui-selenide Pt₂Se₃ layers sandwiched by Ba atoms. Each sesqui-selenide Pt₂Se₃ layer could be considered as a PtSe₂ structure with ordered Se vacancies. It has an atomic coordination within the structure of both the PtSe₆ octahedra and the PtSe₄ square planar, which results in a mixed-valence compound with Pt (II):Pt (IV) = 3:1. It is also interesting to note that the Se atom framework in this compound could be viewed as stacks of distorted Kagome nets formed by Se atoms. We observe a resistivity crossover, mimic to the metal-insulator transition ~150 K and a resistivity plateau at temperatures below 10 K. The X-ray single-crystal diffraction, temperature-dependent electrical resistivity, magnetoresistivity, Hall, effect, heat capacity, and angle-resolved photoemission spectroscopy (ARPES) measurements are carried out to fully characterize this compound and understand the intriguing transport anomalies observed in this system.

¹Department of Physics, The University of Texas at Dallas, Richardson, TX 75080, USA. ²Department of Physics and Astronomy, Rice University, Houston, TX 77005, USA. ³Department of Physics, University of California, Berkeley, CA 94720, USA. ⁴Advanced Light Source, Lawrence Berkeley National Laboratory, Berkeley, CA 94720, USA. ⁵Department of Chemistry, The University of Texas at Dallas, Richardson, TX 75080, USA. ⁶Materials Science Division, Lawrence Berkeley National Laboratory, Berkeley, CA 94720, USA. ⁷School of Physical Science and Technology, Shanghai Tech University, Shanghai 200031, China. ✉email: mingyi@rice.edu; blv@utdallas.edu

Table 1. Crystal structure of BaPt₄Se₆ at room temperature and 100 K.

Temperature	300 K			100 K		
Crystal system	Monoclinic			Monoclinic		
Space group	<i>C2/c</i> (no. 15)			<i>C2/c</i> (no. 15)		
<i>a</i>	12.715(4) Å			12.709(2) Å		
<i>b</i>	7.406(2) Å			7.4004(14) Å		
<i>c</i>	12.461(3) Å			12.406(2) Å		
β	118.089(7)°			118.374(8)°		
<i>Z</i>	4			4		
Atomic position						
Ba1(4c)	1/4	3/4	1/2	1/4	3/4	1/2
Pt1(4e)	0	0.35664(5)	1/4	0	0.35783(4)	1/4
Pt2(4e)	0	0.85699(5)	1/4	0	0.85812(4)	1/4
Pt3(8f)	0.25059(2)	0.59819(3)	0.24539(3)	0.25057(2)	0.59922(3)	0.24530(2)
Se1(8f)	0.03278(6)	0.61103(8)	0.13512(7)	0.03223(5)	0.61205(7)	0.13456(5)
Se2(8f)	0.22316(6)	0.35380(9)	0.36289(7)	0.22376(5)	0.35499(7)	0.36357(5)
Se3(8f)	0.03163(6)	0.10257(8)	0.13610(7)	0.03117(5)	0.10391(7)	0.13565(5)
Absorption coefficient	78.633 mm ^{−1}			79.292 mm ^{−1}		
θ range	3.30–30.57°			3.30–30.54°		
Independent reflections	1599			1575		
Refine Parameters	54			54		
R(int)	0.0564			0.0458		
Final R indices	R ₁ = 0.027, wR ₂ = 0.058			R ₁ = 0.022, wR ₂ = 0.055		
Goodness-of-fit	1.056			1.076		

RESULTS AND DISCUSSIONS

X-ray diffraction and structure description

The details of the X-ray single-crystal refinements and the associated crystallographic parameters for BaPt₄Se₆ at both 300 K and 100 K are provided in Table 1. Additional atomic coordination, selected interatomic distances, angles, and precession images are presented in the supplementary information. In sharp contrast to PtSe₂ in the space group of *P3m1*, BaPt₄Se₆ crystallizes in a distinct structure type (*mC44*) and the centrosymmetric monoclinic space group *C2/c* (#15) with lattice parameters $a = 12.715$ (4) Å, $b = 7.406$ (2) Å, $c = 12.461$ (3) Å, and $\beta = 118.089$ (7)°. The X-ray diffraction pattern with peaks in the preferred orientation is shown in Fig. 1a, together with a photograph of the crystals on the mm scale grid. The crystal structure (Fig. 1b) consists of three distinct Pt sites (Pt1 and Pt2 atoms are at 4e sites and Pt3 atoms are at the general position 8f, as labeled in Fig. 1b). Pt1 atoms at the 4e site are octahedrally coordinated with six neighboring Se atoms and have a formal Pt⁴⁺ valence. The Pt2 atoms at 4e site and the Pt3 atoms at the 8f site, have a square planar environment with nearby Se atoms, and have a formal Pt²⁺ valence (Supplementary Fig. 1). The PtSe₆ octahedra formed by Pt1 atoms are edge shared with the square planar PtSe₄ formed by both Pt2 and Pt3 atoms (Fig. 1b). Each PtSe₆ octahedra is surrounded by six PtSe₄ square planar, and each PtSe₄ square planar is shared by two PtSe₆ octahedra, together they form a sesqui-selenide Pt₂Se₃ layer structure with the stacking along the *c* axis. The interlayer Se–Se distance is 3.478 Å, suggesting weak van der Waals interactions between the sesqui-selenide layers. The Ba atoms are sandwiched between layers and can be charge-balanced as (Ba²⁺) (Pt²⁺)₃(Pt⁴⁺)(Se²⁻)₆ with Pt (II):Pt (IV) = 3:1. The Pt (II)–Se distances in the square planar configuration range from 2.4371(9) Å to 2.4704(9) Å, and are generally shorter than the Pt(IV)–Se distances with octahedral configurations [2.5008(9) Å to 2.5169(9) Å]. Both the PtSe₆ octahedra and PtSe₄ square planar are highly distorted resulting from the monoclinic symmetry of

the crystal structures (Supplementary Fig. 1 and Supplementary Tables 1 and 2).

The sesqui-selenide Pt₂Se₃ layer in this BaPt₄Se₆ compound could be considered as the Se-defect-ordered structure of TMD PtSe₂ layers. Figure 1c represents the projection of the Pt₂Se₃ slab in BaPt₄Se₆. In comparison with the projected monolayer PtSe₂ slab (Fig. 1d), one-third of the Se atomic positions in the Pt₂Se₃ slab remain vacant, as highlighted by red open circles, and the vacancies are alternatively shifted to form a well-ordered honeycomb defect pattern. This ordered vacancy pattern is apparently different from the linear vacancy line pattern observed in the Mo₂S₃ structures and suggests a likely significant change in the electronic structures and transport properties compared with the parent compound PtSe₂.

Electrical transport data and discussions

The temperature-dependent resistivity data of the BaPt₄Se₆ are shown in Fig. 2a. In sharp contrast to the overall semi-metallic behavior of the bulk PtSe₂, this vacancy-ordered sesqui-selenide shows a drastic resistivity crossover at ~150 K with metallic behavior from room temperature down to 150 K and semiconducting behavior below 150 K. Using the thermal activation model formula of $\rho \propto e^{E_a/k_B T}$ within the temperature range from 150 K to 90 K, we obtain an activation energy of 0.82 meV. However, the resistivity begins to deviate from the thermal activation model below 80 K, starts to saturate below 20 K, and reaches a plateau between 10 K and 2 K, reminiscent of the resistivity plateau observed in SmB₆.

Both the resistivity crossover at 150 K and resistivity plateau at lower temperatures are quite intriguing, as they hint at a number of potential causes ranging from a magnetic phase transition, charge density wave (CDW) transition, Kondo effect, topological effects, and localization. We, therefore, carried out temperature-dependent magnetization, single-crystal X-ray diffraction, and heat capacity measurements to further examine the origins of

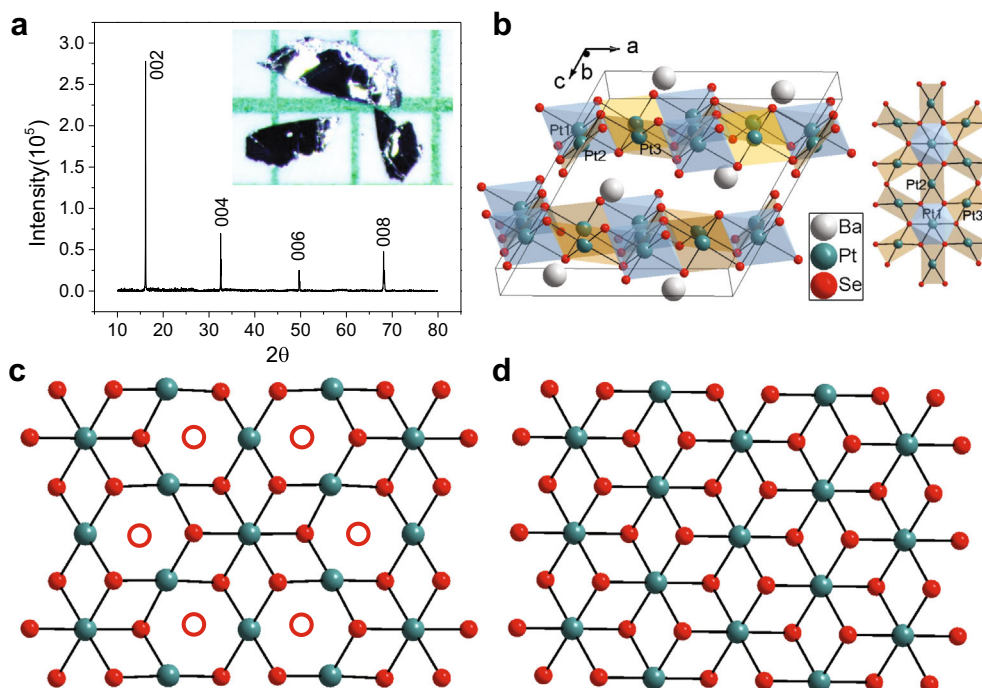


Fig. 1 Structural analysis of the BaPt_4Se_6 . **a** Powder X-ray diffraction on single-crystal with the preferred orientation along c axis, inset is the optical image of the BaPt_4Se_6 single crystals. **b** Side view of BaPt_4Se_6 structure, with the PtSe_6 octahedra and the adjacent PtSe_4 square planar. **c** Projection of the Pt_2Se_3 layer, with the red open circles, denote the vacancy of Se atoms and compare to **d** top view of the PtSe_2 layer from 1T-PtSe_2 .

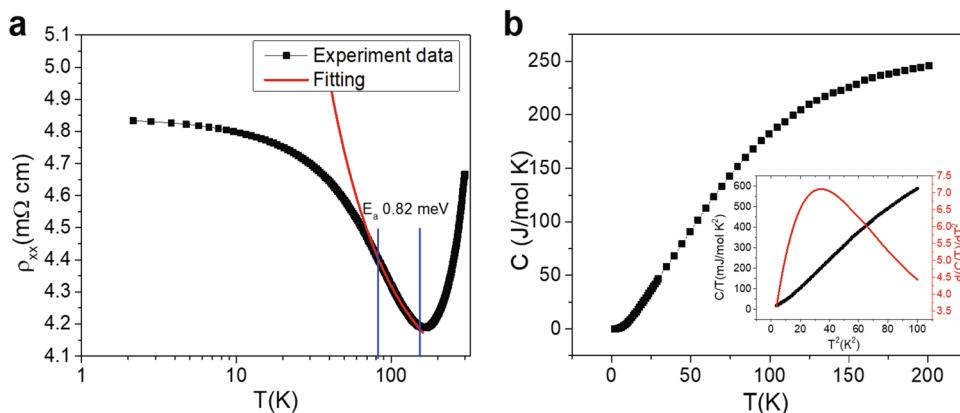


Fig. 2 Electrical resistivity and heat capacity data. **a** Temperature-dependent resistivity in log scale to show the low-temperature resistivity saturation, the red solid line is the fitted data using the activation energy model. **b** Heat capacity of BaPt_4Se_6 from 2 K to 200 K where no clear anomalies or jumps are observed, and the inset is the low-temperature heat capacity and first derivative (in red) data from 2 K to 10 K.

these transport anomalies. First, no magnetic transition is observed from temperature-dependent magnetization measurement (Supplementary Fig. 4). This is consistent with the electron configuration of $5d^8$ for Pt (II) atoms in the square planar coordination and $5d^6$ for Pt (IV) atoms in the octahedral coordination as for both configurations the $5d$ electrons are fully paired. In addition, there are no magnetic ions in this system. Hence, resistivity anomalies cannot be induced by the Kondo effect. Secondly, no clear structural transformation is observed from X-ray single-crystal diffraction in the low-temperature regime down to 100 K. The overnight low-temperature X-ray single-crystal diffraction at 100 K is collected and the refined crystal structures are shown in Table 1. Clearly, no symmetry changes nor splitting of Wyckoff positions is observed between 100 K and 300 K. The integrated precession images that represent the reciprocal space diffraction spots (Supplementary Fig. 2) also do not reflect any

CDW-modulated structural distortions at 100 K compared with the refined structural model at 300 K shown in Table 1. In addition, no clear jumps or anomalies are observed from heat capacity data between 2 K and 200 K (Fig. 2b), which further supports that no structure transition nor other first-order phase transitions exist in this system. Therefore, electron localization is the most likely cause of the resistivity upturn at 150 K in this system. A combination of the thermal activation model and variable range hopping model using different dimension indices to represent the strong localization effect has been used to fit the data between 80 K and 20 K, and yield unreasonably small activation energy <1 μeV . This suggests that weak localization rather than strong localization exists in the system.

Regarding the origin of the resistivity plateau observed at low temperatures, magnetic effects such as the Kondo effect or magnetic field-induced resistivity saturation as observed in WTe_2

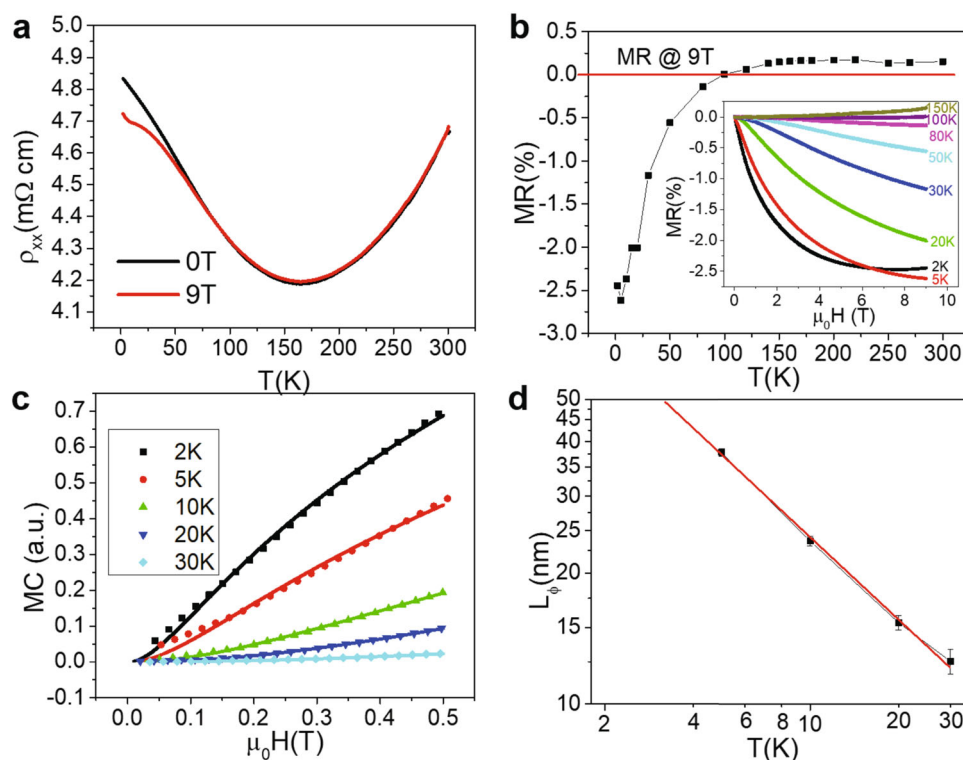


Fig. 3 In-plane magnetoresistivity data and related analysis. **a** Temperature-dependent in-plane resistivity data at zero magnetic field and with the applied magnetic field up to 9 T. **b** Magnetoresistivity at different temperatures under 9 T. The inset shows the isothermal magnetic field-dependent resistivity behavior. **c** Magnetoconductance at low magnetic field range fitted by the HLN formula (solid line) at several temperatures, and **d** Temperature-dependent phase coherence length at different temperatures derived from the HLN formula with linear fitting in the double log scales.

system are not applicable here. One possible explanation could be the contribution of some additional metallic states, which could originate from multiple conducting channels or surface states competing with the localization effects at low temperatures.

The low-temperature range heat capacity data are shown in the inset of Fig. 2b. Interestingly, the heat capacity does not exhibit a linear relationship of C/T vs T^2 following the Debye model $C = \gamma_N T + \beta T^3$ between 2 K and 10 K. By taking the first-order derivative of the nonlinear behavior from 2 K to 10 K, we can clearly observe a broad peak with a maximum at ~ 6 K. This peak may suggest an existing hidden order in the BaPt_4Se_6 system, which could be responsible for the resistivity plateau observed from the electrical resistivity measurement.

Resistivities with and without applying a magnetic field at 9 T in the whole temperature range are shown in Fig. 3a. A clear change of magnetoresistance sign is observed at ~ 100 K, from negative in the low-temperature range to positive in the high-temperature range. The isothermal magnetoresistivity up to 9 T at different temperatures is shown in Fig. 3b, which is consistent with Fig. 3a. Three small yet non-negligible anomalies could be observed: (i) a broad hump at 150 K, which is on par with the M-I transition temperature observed in Fig. 2a; (ii) a change of sign of the magnetoresistance at 100 K from positive to negative is observed; (iii) the magnetoresistance upturn below 5 K. As the localization is typically induced by disorder, the broad hump at 150 K could be explained by the enhanced scattering caused by disorder under magnetic field. However, at low temperatures, a negative magnetoresistivity owing to the localization effect will emerge and become stronger with decreasing temperature. The positive and negative magnetoresistance will compensate each other at intermediate temperatures, which could explain the significant changes of magnetoresistance at ~ 100 K. Below 100 K, the negative magnetoresistance induced by localization becomes

predominant. Interestingly, an upturn of the magnetoresistivity below 5 K is observed, which could also be clearly noticed from the inset of Fig. 3b. In comparison with the 5 K data, the magnetoresistivity at 2 K bends down at high magnetic fields.

In order to demonstrate the weak localization effect in this system, we convert the magnetoresistance data to the magnetoconductance at a low field range with temperatures far below 100 K to minimize the influence of the classical magnetoresistance and fit the data using the Hikami-Larkin-Nagaoka (HLN) formula⁵²

$$\frac{\Delta\sigma(B)}{G_0} = a \left[\Psi\left(\frac{1}{2} + \frac{B_\phi}{B}\right) - \ln\left(\frac{B_\phi}{B}\right) \right] \quad (1)$$

which describes the quantum correction to conductivity owing to weak localization. In the equation $G_0 = e^2/(2\pi^2\hbar)$, a is the parameter in the renormalization group equation, $\Psi(x)$ is the digamma function, $B_\phi = \hbar/(4eL_\phi^2)$ is the characteristic value of the magnetic field with L_ϕ as the phase-coherent length. The fitting results are shown in Fig. 3c, where the data generally are described reasonably well by the HLN formula, some deviation of the fits from experimental values are observed at our lowest measured temperature of 2 K and 5 K, which likely is due to the additional metallic states as seen in the previous resistivity data in Fig. 2a. The phase coherence length L_ϕ extracted from B_ϕ , changes from ~ 47 nm at 2 K to ~ 12 nm at 30 K (Fig. 3d). As we increase temperature, the phase coherence length decreases, typically following the power-law relationship $L_\phi \propto T^{-n}$. As the coherence length value at 2 K is affected by additional metallic states (Fig. 3c), we therefore only perform a linear fitting from 5 K to 30 K (red solid line) (Fig. 3d) and obtain a fitted index of $n = 0.62$ —a value close to $1/2$ indicating the 2D nature of this system.

In order to further understand the carrier contributions at low temperatures for BaPt_4Se_6 , we performed a Hall measurement (Fig. 4a). By sweeping the magnetic field at different temperatures,

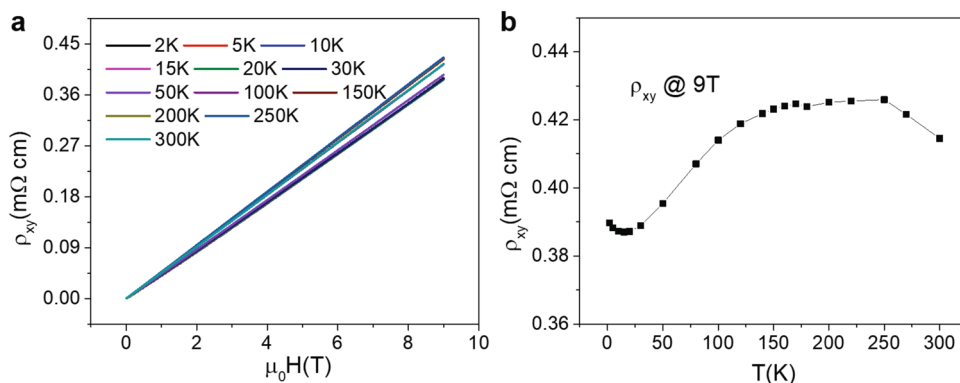


Fig. 4 Hall resistivity data. **a** Field-dependent Hall resistivity of BaPt₄Se₆ at different temperatures up to 9 T. **b** Temperature-dependent Hall resistivity at 9 T.

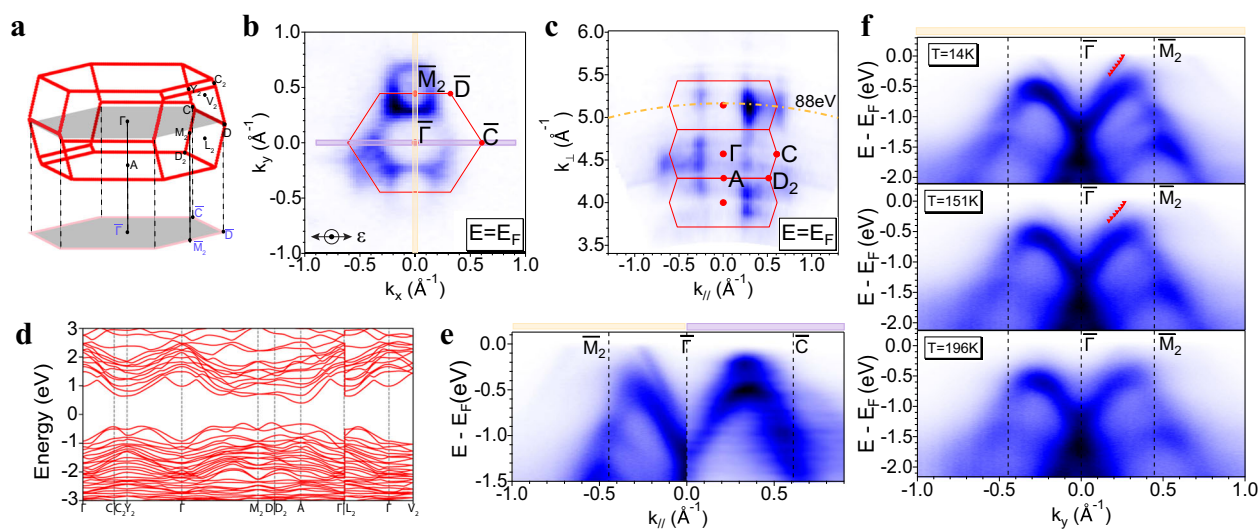


Fig. 5 Angle-resolved photoemission spectroscopy results. **a** 3D BZ of BaPt₄Se₆ where the gray-shaded area denotes the projected (001) surface. **b** FS map integrated within a 2 meV window of the projected (001) surface using 88 eV LH photons at $T = 13.5$ K. Polarization of incident photons is indicated by ϵ . **c** FS map along the k_z direction. **d** DFT calculation for bulk BaPt₄Se₆ with SOC included showing a semiconducting ground state. **e** Band dispersions along the $\bar{\Gamma} - \bar{M}_2$ and $\bar{\Gamma} - \bar{C}$ directions, where the momentum directions have been marked in **b**. **f** Band dispersions along the $\bar{\Gamma} - \bar{M}_2$ direction at 14 K, 151 K, and 196 K, respectively, indicated by a yellow vertical line in panel **b**. Red triangles extracted from MDCs serve as visual guidance for the metallic states crossing the Fermi level.

the Hall resistivity shows a linear relationship with the magnetic field. The Hall resistivity is positive throughout the whole temperature range, suggesting the predominant hole charge carriers in the system. The absolute Hall resistivity value does not change much in the whole temperature range, and the obtained room temperature hole concentration is on the order of 10^{19} cm^{-3} . This is consistent with the resistivity data where no significant change of resistivity is observed despite the M-I transition at 150 K. The temperature-dependent Hall resistivity data at 9 T is shown in Fig. 4b. Both a broad maximum at 150 K and a small upturn below 20 K are observed, consistent with both temperature-dependent resistivity and magnetoresistivity results discussed previously.

Band structure calculations and ARPES measurements

To visualize the electronic structure of BaPt₄Se₆ and its evolution with temperature, we performed ARPES experiments on the high-quality single crystals. From density functional theory (DFT) calculations on the nominal crystal structure, BaPt₄Se₆ is expected to be a semiconductor (Fig. 5d). The measured dispersions, however, indicate a metallic state. To introduce the measured

dispersions, we first show the three-dimensional (3D) Brillouin zone (BZ) notation of BaPt₄Se₆ (Fig. 5a) and the corresponding projected (001) plane sketched in gray and appended to the measured Fermi surface (FS) in Fig. 5b. Note that due to the low symmetry of the BaPt₄Se₆ crystal structure, the FS intensity shows a C_2 symmetric pattern with respect to the $\bar{\Gamma} - \bar{M}_2$ direction only. In the k_z mapping displayed in Fig. 5c, the FS shows an anti-symmetric intensity distribution across k_z , of which the apparent periodicity is twice that of the BZ size. Such observed intensity pattern is owing to the structural factor originating from the two stacked Pt₄Se₆ layers within each unit cell. Consequently, the k_z FS mapping intensity manifests more strongly the periodicity of the single-layer Pt₄Se₆. The measured FS shows Fermi pockets around the BZ boundaries. Along $\bar{\Gamma} - \bar{M}_2$, we observe these pockets to be small hole pockets from two linear bands crossing the Fermi level consistent with a metallic nature, albeit near the valence band top (Fig. 5e). From a comparison with the calculation, we observe that the bands away from Fermi level present better consistencies with the calculation. The origin of the mismatch here is likely owing to Se vacancies in the material that slightly hole-dopes the sample. The electronic dispersions of BaPt₄Se₆ indicate a degree of

resemblance to that of PtSe_2 , albeit with distinction. The dispersions at the $\bar{\Gamma}$ point emerge from an X-shape feature at ~ -1.3 eV (Fig. 5f top figure and Supplementary Fig. 5). A pair of bands are observed at the \bar{M}_2 point, which in PtSe_2 are observed to carry spin texture owing to Rashba splitting⁴⁵. However, the measured FS and dispersions show much lower symmetry compared with PtSe_2 .

We also carried out temperature-dependent measurements to examine the connection to the transport anomalies. The middle panel in Fig. 5f shows the $\bar{\Gamma} - \bar{M}_2$ cut at 151 K corresponding to the M-I transition shown above, while the figure at the bottom is taken at a temperature high above the transition. Evidently, considering thermal broadening, major features of the band structure, especially the bands crossing Fermi level remain largely unchanged between 14 K and 196 K. The red triangles in Fig. 5f are fitted from momentum distribution curves (MDCs) to highlight the band crossing the Fermi level. Our observation supports the argument that the resistivity crossover ~ 150 K is not caused by any change of the density of states near E_F , but according to the analysis above can be attributed to the weak localization effect.

In summary, A layered ternary compound BaPt_4Se_6 has been discovered with sesqui-selenide layered feature and mix-valence Pt oxidation states. The sesqui-selenide layer is similar to the TMD PtSe_2 structure with ordered Se vacancies. Electrical resistivity measurements reveal two transport anomalies: one resistivity crossover at ~ 150 K and a resistivity plateau below 10 K. Extensive studies from X-ray diffraction and heat capacities suggest the resistivity crossover is due to weak localization that is related to the structural distortion and ordered honeycomb Se vacancy of the structure. Temperature-dependent ARPES measurements reveal a metallic state between 14 K and 196 K, and do not show any abrupt electronic changes in the whole temperature range, further supporting the weak localization effect in this compound. Magnetoresistivity, Hall, and heat capacity measurements concurrently suggest an existing hidden state below 5 K, which should be responsible for the resistivity plateau at low temperatures. The hole-like band in the MDC curves from the ARPES measurements is consistent with hole charge carriers from our Hall data. Unfortunately, no clear evidence of the existence of the in-gap state is observed from ARPES measurements down to 14 K, which is slightly higher than the resistivity plateau below 10 K. The exact origin of the emerged metallic ground state at low temperatures is responsible for the resistivity plateau is subject for future studies.

METHODS

Material synthesis and X-ray diffraction

The compound was initially discovered during the chemical doping studies for Ba_xPtSe_2 . The small grain crystals are isolated first for chemical analysis and initial X-ray diffraction studies. The large size of single crystals of BaPt_4Se_6 was later directly synthesized through solid-state reaction using Ba pieces (99.9%, Alfa Aesar), Pt pieces (99%), and Se shots (99.999%, Alfa Aesar). A stoichiometric amount of the starting materials were placed into a graphite crucible and then sealed in the fused quartz tube under a vacuum. The tube was placed in a furnace, slowly heat with a rate of $30^\circ\text{C}/\text{h}$ up to 1100°C , and maintained for 48 hours before slowly cooled down to 800°C with the rate of $3^\circ\text{C}/\text{h}$. Thin shining black crystals can be obtained by carefully cleaving the melt ingot and with preferred c axis orientations (Fig. 1a). The exact crystal structure was determined by Bruker D8 Quest Kappa single-crystal X-ray diffractometer equipped with a Mo $\text{K}\alpha$ $\text{I}\mu\text{S}$ microfocus source ($\lambda = 0.71073 \text{ \AA}$) operating at 50 kV and 1 mA with a HELIOS optic monochromator and a CMOS detector. The collected data set was integrated with Bruker SAINT and scaled with Bruker SADABS (multiscan absorption correction). The refined chemical composition from single-crystal diffraction was subsequently confirmed by scanning electron microscope energy-dispersive X-ray spectroscopy (Supplementary Fig. 3).

Physical properties measurements

The electric resistivity and Hall coefficient were measured by employing the standard six probe method using golden wires and silver paste on a $2 \times 1 \times 0.1 \text{ mm}^3$ crystal with the temperature down to 2 K and magnetic field up to 9 T. The magnetoresistivity measurement using standard six probe method with magnetic field perpendicular to the crystal plane and current, the heat capacity measurement using the relaxation method down to 2 K, were performed in a Quantum Design Physical Property Measurement System. ARPES measurements were performed at the MERLIN beamline 4.0.3 at the Advanced Light Source, equipped with a SCIENTA R8000 electron analyzer. The single crystal was cleaved in situ at 13 K and measured in an ultra-high vacuum with a base pressure better than 5×10^{-11} Torr. Photon energy-dependent measurements were carried out from 30 to 120 eV, and 88 eV linear horizontal light was selected to obtain the highest data quality.

Electronic structure calculations

The electronic structure of BaPt_4Se_6 was calculated in the framework of DFT within the generalized gradient approximation⁵³. The projector-augmented-wave method implemented in Vienna Ab Initio Simulation Package is employed with the default energy cutoff specified in the pseudopotential file. The momentum grid is taken as $9 \times 9 \times 9$. The SOC is included in the calculation self-consistently. The calculations are performed at the HPC Platform of ShanghaiTech University Library and Information Services and the School of Physical Science and Technology.

DATA AVAILABILITY

The authors declare that all essential data supporting the findings of this study are available within the paper and its supplementary information.

Received: 23 April 2021; Accepted: 1 September 2021;

Published online: 23 September 2021

REFERENCES

- Splendiani, A. et al. Emerging photoluminescence in monolayer MoS_2 . *Nano Lett.* **10**, 1271–1275 (2010).
- Jaramillo, T. F. et al. Identification of active edge sites for electrochemical H_2 evolution from MoS_2 nanocatalysts. *Science* **317**, 100–102 (2007).
- Deng, K. et al. Experimental observation of topological Fermi arcs in type-II Weyl semimetal MoTe_2 . *Nat. Phys.* **12**, 1105–1110 (2016).
- Wang, Z. et al. MoTe_2 : a type-II Weyl topological metal. *Phys. Rev. Lett.* **117**, 056805 (2016).
- Tang, S. et al. Quantum spin Hall state in monolayer $1\text{T}'\text{-WTe}_2$. *Nat. Phys.* **13**, 683–687 (2017).
- Wang, Y. et al. Structural phase transition in monolayer MoTe_2 driven by electrostatic doping. *Nature* **550**, 487–491 (2017).
- Zhao, C. et al. Enhanced valley splitting in monolayer WSe_2 due to magnetic exchange field. *Nat. Nanotechnol.* **12**, 757–762 (2017).
- Fatemi, V. et al. Electrically tunable low-density superconductivity in a monolayer topological insulator. *Science* **362**, 926–929 (2018).
- Xu, S.-Y. et al. Electrically switchable Berry curvature dipole in the monolayer topological insulator WTe_2 . *Nat. Phys.* **14**, 900–906 (2018).
- Sajadi, E. et al. Gate-induced superconductivity in a monolayer topological insulator. *Science* **362**, 922–925 (2018).
- Hou, W. et al. Strain-based room-temperature non-volatile MoTe_2 ferroelectric phase change transistor. *Nat. Nanotechnol.* **14**, 668–673 (2019).
- Yu, W. et al. Chemically exfoliated VSe_2 monolayers with room-temperature ferromagnetism. *Adv. Mater.* **31**, 1903779 (2019).
- Choi, Y.-B. et al. Evidence of higher-order topology in multilayer WTe_2 from Josephson coupling through anisotropic hinge states. *Nat. Mater.* **19**, 974–979 (2020).
- Wang, W. et al. Evidence for an edge supercurrent in the Weyl superconductor MoTe_2 . *Science* **368**, 534–537 (2020).
- Ali, M. N. et al. Large, non-saturating magnetoresistance in WTe_2 . *Nature* **514**, 205–208 (2014).
- Liu, W. et al. Enhanced superconductivity in the Se-substituted 1T-PdTe_2 . *Phys. Rev. Mater.* **5**, 014802 (2021).
- Wu, H. et al. Spacing dependent and doping independent superconductivity in intercalated 1T two dimensional SnSe_2 . *2D Mater.* **6**, 045048 (2019).

18. Zhang, C. et al. Strain distributions and their influence on electronic structures of $\text{WSe}_2\text{-MoS}_2$ laterally strained heterojunctions. *Nat. Nanotechnol.* **13**, 152–158 (2018).
19. Edelberg, D. et al. Approaching the intrinsic limit in transition metal diselenides via point defect control. *Nano Lett.* **19**, 4371–4379 (2019).
20. Yu, Z. et al. Analyzing the carrier mobility in transition-metal dichalcogenide MoS_2 field-effect transistors. *Adv. Funct. Mater.* **27**, 1604093 (2017).
21. Lin, Z. et al. Defect engineering of two-dimensional transition metal dichalcogenides. *2D Mater.* **3**, 022002 (2016).
22. Wang, X. et al. Deriving 2D M_2X_3 ($\text{M} = \text{Mo, W}$, $\text{X} = \text{S, Se}$) by periodic assembly of chalcogen vacancy lines in their MX 2 counterparts. *Nanoscale* **12**, 8285–8293 (2020).
23. Liang, Q., Zhang, Q., Zhao, X., Liu, M. & Wee, A. T. S. Defect engineering of two-dimensional transition-metal dichalcogenides: applications, challenges, and opportunities. *ACS Nano* **15**, 2165–2181 (2021).
24. Liu, E. et al. Giant anomalous Hall effect in a ferromagnetic kagome-lattice semimetal. *Nat. Phys.* **14**, 1125–1131 (2018).
25. Little, A. et al. Three-state nematicity in the triangular lattice antiferromagnet $\text{Fe}_{1/3}\text{NbS}_2$. *Nat. Mater.* **19**, 1062–1067 (2020).
26. Zhu, H. et al. New Mo_6Te_6 Sub-nanometer-diameter nanowire phase from 2H- MoTe_2 . *Adv. Mater.* **29**, 1606264 (2017).
27. Tiwari, R. K., Yang, J., Saeys, M. & Joachim, C. Surface reconstruction of MoS_2 to Mo_2S_3 . *Surf. Sci.* **602**, 2628–2633 (2008).
28. Avsar, A. et al. Defect induced, layer-modulated magnetism in ultrathin metallic PtSe_2 . *Nat. Nanotechnol.* **14**, 674–678 (2019).
29. Zhang, J. et al. Distorted monolayer ReS_2 with low-magnetic-field controlled magnetoelectricity. *ACS Nano* **13**, 2334–2340 (2019).
30. Jung, Y., Zhou, Y. & Cha, J. J. Intercalation in two-dimensional transition metal chalcogenides. *Inorg. Chem. Front.* **3**, 452–463 (2016).
31. Zhang, Q., Mei, L., Cao, X., Tang, Y. & Zeng, Z. Intercalation and exfoliation chemistries of transition metal dichalcogenides. *J. Mater. Chem. A* **8**, 15417–15444 (2020).
32. Wang, Z., Li, R., Su, C. & Loh, K. P. Intercalated phases of transition metal dichalcogenides. *SmartMat* **1**, e1013 (2020).
33. Novello, A. M. et al. Stripe and short-range order in the charge density wave of 1T- Cu_xTiSe_2 . *Phys. Rev. Lett.* **118**, 017002 (2017).
34. Liao, J.-H., Zhao, Y.-C., Zhao, Y.-J., Yang, X.-B. & Chen, Y. Doping induced charge density wave in monolayer TiS_2 and phonon-mediated superconductivity. *J. Appl. Phys.* **127**, 044301 (2020).
35. Bhoi, D. et al. Interplay of charge density wave and multiband superconductivity in 2H- Pd_xTaSe_2 . *Sci. Rep.* **6**, 24068 (2016).
36. Zhu, L. et al. Superconductivity in potassium-intercalated $\text{T}_d\text{-WTe}_2$. *Nano Lett.* **18**, 6585–6590 (2018).
37. Nair, N. L. et al. Electrical switching in a magnetically intercalated transition metal dichalcogenide. *Nat. Mater.* **19**, 153–157 (2020).
38. Sanikop, R., Budumuru, A. K., Gautam, S., Chae, K. H. & Sudakar, C. Robust ferromagnetism in Li-intercalated and-deintercalated MoS_2 nanosheets: implications for 2D spintronics. *ACS Appl. Nano Mater.* **3**, 11825–11837 (2020).
39. Yim, C. et al. High-performance hybrid electronic devices from layered PtSe_2 films grown at low temperature. *ACS Nano* **10**, 9550–9558 (2016).
40. Chia, X. et al. Layered platinum dichalcogenides (PtS_2 , PtSe_2 , and PtTe_2) electrocatalysis: monotonic dependence on the chalcogen size. *Adv. Funct. Mater.* **26**, 4306–4318 (2016).
41. Wang, Z., Li, Q., Besenbacher, F. & Dong, M. Facile synthesis of single crystal PtSe_2 nanosheets for nanoscale electronics. *Adv. Mater.* **28**, 10224–10229 (2016).
42. Li, Y. et al. Topological origin of the type-II Dirac fermions in PtSe_2 . *Phys. Rev. Mater.* **1**, 074202 (2017).
43. Zhang, K. et al. Experimental evidence for type-II Dirac semimetal in PtSe_2 . *Phys. Rev. B* **96**, 125102 (2017).
44. Zhao, Y. et al. High-electron-mobility and air-stable 2D layered PtSe_2 FETs. *Adv. Mater.* **29**, 1604230 (2017).
45. Yao, W. et al. Direct observation of spin-layer locking by local Rashba effect in monolayer semiconducting PtSe_2 film. *Nat. Commun.* **8**, 14216 (2017).
46. Wang, Y. et al. Monolayer PtSe_2 , a new semiconducting transition-metal-dichalcogenide, epitaxially grown by direct selenization of Pt. *Nano Lett.* **15**, 4013–4018 (2015).
47. Zheng, H. et al. Visualization of point defects in ultrathin layered 1T- PtSe_2 . *2D Mater.* **6**, 041005 (2019).
48. Shawkat, M. S. et al. Thickness-independent semiconducting-to-metallic conversion in wafer-scale two-dimensional PtSe_2 layers by plasma-driven chalcogen defect engineering. *ACS Appl. Mater. Interfaces* **12**, 14341–14351 (2020).
49. Absor, M. A. U. et al. Defect-induced large spin-orbit splitting in monolayer PtSe_2 . *Phys. Rev. B* **96**, 115128 (2017).
50. Sajjad, M., Singh, N. & Schwingenschlögl, U. Strongly bound excitons in monolayer PtS_2 and PtSe_2 . *Appl. Phys. Lett.* **112**, 043101 (2018).
51. Xu, H. et al. Controlled doping of wafer-scale PtSe_2 films for device application. *Adv. Funct. Mater.* **29**, 1805614 (2019).
52. Hikami, S., Larkin, A. I. & Nagaoka, Y. Spin-orbit interaction and magnetoresistance in the two-dimensional random system. *Prog. Theor. Phys.* **63**, 707–710 (1980).
53. Perdew, J. P., Burke, K. & Ernzerhof, M. Generalized gradient approximation made simple. *Phys. Rev. Lett.* **77**, 3865 (1996).

ACKNOWLEDGEMENTS

This work at the University of Texas at Dallas is supported by the US Air Force Office of Scientific Research grant no. FA9550-19-1-0037. This project is also partially funded by NSF-DMREF-1921581, and the University of Texas at Dallas Office of Research through the Seed Program for Interdisciplinary Research (SPIRe) and Core Facility Voucher Program. J.Y.C. also acknowledges partial support from NSF-DMR-1700030. Work at Rice University was supported by the Gordon and Betty Moore Foundation's EPIQS Initiative through grant No. GBMF9470, the Robert A. Welch Foundation grant no. C-2024, the Alfred P. Sloan Foundation, as well as in part by NSF-DMREF-1921847. Work at UC Berkeley is funded by NSF-DMR-1921798. This research used resources of the Advanced Light Source, a U.S. DOE Office of Science User Facility under contract no. DE-AC02-05CH11231.

AUTHOR CONTRIBUTIONS

B.L. conceived and initiated this project, S.L., H.W., H.Z., W.L. and D.P.P. performed the sample growth and transport data measurements, Y.Z. and J.S.O. performed the ARPES experiments with the help of J.D. under the guidance of R.J.B. and M.Y., G.T.M. performed the single-crystal X-ray diffraction experiments, G.L. performed the theoretical calculations. S.L., M.Y. and B.L. wrote the paper with input from all authors.

COMPETING INTERESTS

The authors declare no competing interests.

ADDITIONAL INFORMATION

Supplementary information The online version contains supplementary material available at <https://doi.org/10.1038/s41535-021-00382-x>.

Correspondence and requests for materials should be addressed to Ming Yi or Bing Lv.

Reprints and permission information is available at <http://www.nature.com/reprints>

Publisher's note Springer Nature remains neutral with regard to jurisdictional claims in published maps and institutional affiliations.



Open Access This article is licensed under a Creative Commons Attribution 4.0 International License, which permits use, sharing, adaptation, distribution and reproduction in any medium or format, as long as you give appropriate credit to the original author(s) and the source, provide a link to the Creative Commons license, and indicate if changes were made. The images or other third party material in this article are included in the article's Creative Commons license, unless indicated otherwise in a credit line to the material. If material is not included in the article's Creative Commons license and your intended use is not permitted by statutory regulation or exceeds the permitted use, you will need to obtain permission directly from the copyright holder. To view a copy of this license, visit <http://creativecommons.org/licenses/by/4.0/>.

© The Author(s) 2021